Improving the corrosion resistance of ferritic-martensitic steels at 600°C in molten solar salt via diffusion coatings

Tobias M. Meißner[A*1], Ceyhun Oskay [A], Alexander Bonk[B], Benjamin Grégoire[A], Alexander Donchev[A], Ali Solimani[A], Mathias C. Galetz[A*2]

[A] DECHEMA-Forschungsinstitut, 60486 Frankfurt am Main, Germany
[B] German Aerospace Center (DLR), Institute of Engineering Thermodynamics, 70569 Stuttgart, Germany

*1 *Corresponding author:* tobias.marc.meissner@gmail.com
*2 *Second correspondence:* mathias.galetz@dechema.de

Keywords:
Concentrated solar power (CSP), Salt chemistry, Molten nitrate corrosion, Ferritic-martensitic steel, Diffusion coatings, Nickel electroplating

ABSTRACT
Molten salt corrosion in the receiver's piping system and storage tanks is still one of the major drawbacks of concentrated solar power (CSP) plants and is currently covered by using expensive high-alloyed steels or Ni-base alloys. The employment of cheaper structural materials combined with protective coatings is an attractive alternative to increase cost-efficiency. The present study investigates the corrosion resistance of three different coatings (a pure Ni, a Cr and a combined Ni+Cr coating) deposited on ferritic-martensitic X20CrMoV12-1 steel during isothermal immersion in molten solar salt in comparison to uncoated Ni-base alloy Haynes 230. Exposure tests were conducted at 600°C for up to 1000 h. To identify the individual role of the main elements, exposure tests of pure Fe, Ni and Cr were undertaken as well. In addition to the cross-sectional investigations via light-optical microscopy and EPMA, X-ray diffraction measurements were conducted to identify the corrosion products. These were complemented by weight change measurements and chemical analysis of the salts after the exposure tests.
The study reveals differences between the corrosion behaviour of the different coating approaches, which is discussed as a function of coating composition and degradation mechanisms. Whereas pure Cr or pure Ni coatings offer hardly any improved protection of the uncoated X20CrMoV12-1 substrate, the combined Ni+Cr coating performs very well and improves the scaling behaviour of X20CrMoV12-1 significantly. The outcome highlights the correlation between the solubility of the pure metals Fe, Ni and Cr in molten solar salt and the corrosion resistance of the investigated coatings.

1. Introduction

During the past years, efforts to counteract the human-induced climate changes have been drastically increased. A major goal is the reduction of overall CO_2-emissions, which is addressed e.g. by shutting down conventionally coal-fired power plants and replacing them by renewable energy sources. A particularly high potential is attributed to the exploitation of solar energy, which can be converted to electricity either by means of photovoltaics or by solar-thermal conversion. In the so-called concentrated solar power (CSP) tower plants, solar radiation is concentrated onto a central receiver by a field of programmable heliostats. A heat transfer fluid (HTF) is circulated through the piping system of the receiver and transfers the thermal energy to a conventional water-steam circuit to produce electricity. In CSP plants of recent design molten salts are typically used as HTF owing to their excellent heat storage potential. In combination with a thermal energy storage system (TES), the CSP technology can offer continuous power supply and is qualified to replace the capacity formerly provided by fossil fuel-fired power plants [1]. However, the energy conversion efficiency (η) of state-of-the-art CSP plants lies around 25% [2,3] and is inferior compared to conventional energy generation methods [4,5]. This leads to higher cost of electricity generated by the CSP technology and decreases its competitiveness [6–8].

The overall efficiency of the CSP technology can be increased by optimising various system components such as the central receiver and the HTF. One possibility to optimise the receiver system is to increase the solar absorptance of the exterior surfaces of the absorber panels while decreasing their thermal emittance, which is commonly realised by means of exterior absorber coatings [9–11]. Regarding HTFs, potential for optimisation lies in their thermo-physical characteristics such as high heat capacity, high thermal stability and low viscosity [2,12,13]. Currently, the non-eutectic salt mixture of 60 wt.% $NaNO_3$ – 40 wt.% KNO_3 known as "solar salt" is widely employed as the state-of-the-art HTF due to its beneficial thermo-physical properties [12,14,15]. However, one major drawback restricting the maximum operation temperature of the receiver system is the low thermal stability limit of this nitrate mixture: At temperatures exceeding 600°C rapid thermal decomposition of the nitrate anions into nitrite anions and, subsequently, into soluble oxide ions and gaseous nitrous oxides occurs (see reactions (1) and (2)) [16,17].

$$NO_3^- \rightleftharpoons NO_2^- + \frac{1}{2}O_2(g) \tag{1}$$

$$2NO_2^- \rightleftharpoons NO_2(g) + NO(g) + O^{2-} \tag{2}$$

Such reactions alter the chemical composition and the thermo-physical properties of the molten salt. More importantly, they result in increased amounts of oxidising agents and corrosive species in the salt melt [2,18–20].

Due to the above stated reasons, corrosion resistance of structural materials employed in the receiver piping system is a determining factor for plant design and lifetime. Compared to steels, Ni-base alloys such as Haynes 230 offer an improved corrosion behaviour and are therefore typically selected as tube material in the hot sections of the piping system [14]. Since these materials are comparatively expensive, economic considerations would favour the employment of cheaper ferritic-martensitic steels. They offer a much better heat transfer behaviour [21,22], a lower coefficient of thermal expansion (CTE) [21] and still possess adequate creep strength in the

relevant temperature range for CSP applications [23,24]. Although their employment as structural materials would lead to a significant increase in the cost-efficiency of the CSP technology, their low corrosion resistance in these particular environments limits their applicability [15,19,25].

In order to overcome this restriction, a number of anticorrosion methods have recently been explored such as salt purification [26], controlling the process atmosphere [27] or alloy surface graphitisation [28]. Another possible solution is the application of protective coatings on surfaces which are in direct contact with the molten salt. Aluminisation is an industrially well-known coating process leading to the formation of Fe-Al intermetallics [29–32]. Despite the excellent molten nitrate corrosion behaviour of Fe aluminides [33], such ordered intermetallic phases are inherently brittle [34]. Moreover, their higher CTE in relation to the ferritic-martensitic substrate [35–37] could lead to the formation of cracks lowering the creep and thermal fatigue strength of structural components [38,39].

The present work proposes the surface enrichment with Ni and/or Cr: On the one hand, the positive effect of Ni on corrosion resistance in molten nitrates is highlighted by the typically higher corrosion resistance of Ni-base alloys over austenitic steels and over ferritic-martensitic materials [25,40]. Cr on the other hand, despite generally being a stable oxide former in various industrial applications, is prone to be leached from alloys and scales to the nitrate melt [20,33,41]. Nonetheless, enrichment of Cr at the alloy surface helps to delay the transition of structural materials into breakaway corrosion during immersion in solar salt [25]. Considering all described effects of Ni and Cr, the present paper proposes surface modification by 3 different coatings to improve the corrosion resistance of ferritic-martensitic X20CrMoV12-1 steel: (i) a pure "Ni coating" prepared by conventional electrochemical methods, (ii) a "Cr coating" manufactured via the industrially well-established Cr pack cementation process and (iii) a "Ni+Cr coating" via a combination of both processes. The Ni+Cr coating is based on preliminary Ni electroplating and aims at the combined use of Ni and Cr to profit from the beneficial impact on corrosion resistance attributed to each of these elements.

In order to verify the applicability of the three coatings, their corrosion behaviour is investigated in CSP-relevant conditions and compared to the uncoated ferritic-martensitic base material as well as high-grade Ni-base alloy Haynes 230. An additional focus is set on the isolated role of the coating components Ni, Fe and Cr, which is elucidated by investigating the corrosion behaviour of pure metal specimens and the changes in salt chemistry over time.

2. Materials and Methods

2.1 Sample preparation

Ferritic-martensitic steel of type X20CrMoV12-1 (hereafter abbreviated as X20) was used as base material for coating application. The Ni-base alloy Haynes 230 was employed as a reference, since it is used in thermally stressed sections of the CSP absorber tubing of recent design [14]. Chemical compositions of both alloys are shown in Table 1.

Table 1: Nominal chemical composition of alloys used in this study [42,43].

	Material composition [wt.%]													
	Fe	*C*	*Cr*	*Ni*	*Mn*	*Mo*	*Si*	*Al*	*V*	*Cu*	*P*	*S*		
X20CrMoV12-1	bal.	0.17-0.23	10-12.5	0.3-0.8	0.3-1	0.8-1.2	≤0.4	≤0.04	0.2-0.35	≤0.3	≤0.025	≤0.015		
	Fe	*C*	*Cr*	*Ni*	*Mn*	*Mo*	*Si*	*Al*	*W*	*Co*	*Nb*	*Ti*	*La*	*B*
Haynes 230	≤3.0	0.1	22.0	bal.	0.5	2.0	0.4	0.3	14.0	≤5.0	≤0.5	≤0.1	0.02	≤0.015

The alloys were first machined into coupons of size 15x10x3 mm^3 by wire cutting. In the case of X20 samples, a hole was drilled in each coupon to allow for a more convenient application of the coatings. Afterwards, the rectangular test pieces were ground to 320 grit with SiC paper to remove native oxides. Additionally, they were glass-bead blasted to achieve industrially relevant surface conditions and ultrasonically degreased in acetone to remove contaminations. Moreover, in order to determine their mass change, all test samples were weighed following each coating step and prior to exposure using a precision weighing balance (0.01 mg, Mettler Toledo XP205, Columbus, USA). Additionally, their dimensions were measured followed by a calculation of each sample's individual surface area to finally assess specific weight changes.

2.2 Coating manufacturing

Three different coatings were applied onto the ferritic-martensitic substrate: a "Ni coating", a "Cr coating" and a "Ni+Cr coating".

The "Ni coating" was manufactured by means of conventional electrodeposition of Ni at room temperature using an electrolyte consisting of 20.4 wt.% $Ni(SO_3NH_2)_2$, 3.1 wt.% $NiCl_2$ and 3.1 wt.% H_3BO_3 dissolved in distilled water (73.4 wt.%). The process time was 8 h while the solution was homogenised with a magnetic stirrer (stirring speed 100 rpm) and the electrical current was set to 100 mA.

The "Cr coating" and the "Ni+Cr coating" were both manufactured via the industrially well-established Cr powder pack cementation process [44–46] on the basis of either pure X20CrMoV12-1 or galvanically Ni-coated X20CrMoV12-1 prior to the diffusion process, respectively. The process parameters utilised were as follows: 1050°C for 2 h under flowing Ar+5 vol.% H_2 with a powder mixture comprising 5 wt.% Cr (master alloy), 2 wt.% $MnCl_2$ (activator), 93 wt.% Al_2O_3 (inert filler).

2.3 Setup for exposure to molten salt

2.3.1 Exposure of alloys and coatings

For the isothermal exposure tests solar salt was prepared from high-purity $NaNO_3$ (60 wt.%, BASF Group) and KNO_3 (40 wt.%, Haifa Chemicals). The salt mixture was homogenised for 2 h with a planetary mixer. Exposure tests were conducted at 600°C for 100 h, 300 h and 1000 h in a horizontal tube furnace in an atmosphere of flowing (dry) synthetic air (4 l/h). The test temperature was chosen as the upper limit and the target of current attempts to improve CSP system efficiency, respectively. A recent study underlines the prospect of molten solar salt to be reasonably used even at such high temperatures [27]. A schematic of the experimental setup is illustrated in Fig. 1. The exposure tests were carried out placing the test specimens in individual cylindrical crucibles and covering them with the salt mixture, generally following the specifications of ISO 17245:2015 [47]. After each time interval a sample of both substrates as well as one sample per coating type was removed from the hot furnace, cooled to room temperature, carefully rinsed in warm water to remove salt remnants and weighed.

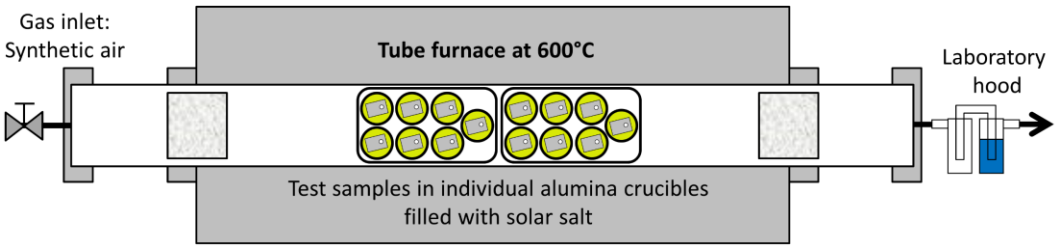

Fig. 1: Schematic drawing of the corrosion test rig.

2.3.2 Exposure of pure metals

In order to fundamentally investigate the solubility behaviour of major alloying and coating elements in nitrate melts, metallic coupon specimens (20x10x3 mm^3) of pure Fe (>99.8%, REMAG AG), Ni (99.99%, Goodfellow GmbH) and Cr (99.95%, Plansee SE) were exposed to molten solar salt. The setup used has been described in length elsewhere [48]. In short, a modified convection furnace was used which fits up to nine alumina crucibles. The configuration allows crucibles to reach out of the furnace and to be passively cooled, thereby supressing salt creeping over the course of the experiment. Each crucible is sealed with a flange containing multiple openings for thermocouples, gas inlet, gas outlet and sample extraction. Every metal sample was placed in an individual crucible to avoid galvanic corrosion. Salt samples were extracted from each crucible after 24 h, 48 h, 72 h and 96 h.

2.4 Characterisation methods

2.4.1 Sample characterisation

Phase analysis of the cleaned samples was conducted via X-ray diffractometry (XRD) using a Bruker D8 diffractometer in Bragg-Brentano configuration with Cu $K\alpha_1$ radiation (0.15406 nm) and equipped with a Lynxeye-semiconductor detector.
In order to enhance the contrast between corrosion or oxidation products and the adjacent epoxy resin, the samples were carefully wrapped in Ni foil prior to the mounting in hot resin. Afterwards, cross sections of all test specimens were prepared by conventional metallographic methods which involve grinding with successively finer SiC paper up to 1200 grit and polishing with 3 µm and 1 µm diamond suspensions. Inspection of the cross sections was then carried out with the help of standard micro-analytical methods such as optical light microscopy, scanning electron microscopy (SEM, Philips XL-40) and complementary electron probe microanalysis (EPMA) measurements with a JEOL JXA-8100.

2.4.2 Salt characterisation

The salt samples extracted from all experiments were analysed in terms of anion composition of nitrate, nitrite, oxide ions, chromate and, for the experiments with pure metals, also in terms of cation (Ni, Cr, Fe) content. Ion chromatography (IC) was performed using a Metrohm IC (883 Basic IC plus) to quantify the levels of nitrate, nitrite and chromate species. A statistical analysis of the system is described elsewhere [48]. The concentrations of Ni, Cr and Fe in the salt were determined using flame atomic absorption spectroscopy (FAAS, Thermo Fisher iCE 3000) with quadline deuterium arc background correction. Hollow cathode lamps were used as the radiation sources at 248.3 nm (Fe), 357.9 nm (Cr) and 232.0 nm (Ni) with a 0.2 nm slit width. Acetylene flow rates of 0.9 l/min (Fe), 4.7 l/min (Si) and 4.3 l/min (Al) were employed. Air-acetylene flames (Fe detection) or nitrous oxide (N_2O)-acetylene flames (Si, Al detection) were used with automatically adjusted air/N_2O flow rates to meet stoichiometric flame conditions. Calibration was performed in a range of 1 mg/l to 5 mg/l for each cation with quadratic fit functions and the regression fits had a coefficient of determination of at least $R^2 = 0.9997$.

3. Results and Discussion

3.1 Microstructure of as-deposited coatings

Cross sections of the three resulting coatings in the as-deposited condition are shown in Fig. 2a to c, respectively.

The electroplated Ni coating, Fig. 2a, has a thickness of approximately 15-20 µm (variations originate from electric field inhomogeneities during deposition).

Cross-sectional characterisation of the Cr coating, Fig. 2b, reveals the presence of a $Cr_{23}C_6$ top layer (confirmed via XRD analysis, not shown here) with a thickness of approximately 8 µm. Its formation can be explained by the high activity of Cr at the powder mixture-substrate interface together with a high mobility of C in X20 at the coating manufacturing temperature of 1050°C, which resulted in Cr inward and C outward diffusion. A similar microstructure was observed by Zancheva et al. [49] after chromising a carbon steel with a comparable content of 0.2 wt.% C. Underneath the carbide layer, a thin ferritic diffusion zone formed, in which inward diffusing Cr is enriched up to a maximum content of 15 wt.%.

The morphology of the combined Ni+Cr coating, Fig. 2c, is likewise characterised by a $Cr_{23}C_6$ top layer above a diffusion zone. The presence of a carbide layer, although it is slightly thinner with an approximate thickness of 2 to 5 µm, indicates outward diffusion of C from the substrate through the deposited Ni layer during pack cementation. The Ni layer, initially pure in composition prior to pack cementation, transformed into a large austenitic diffusion zone of 25 to 30 µm thickness. It is enriched in Fe (originating from the substrate, resulting in Kirkendall porosity to some extent) and Cr (originating from the substrate and from the pack cementation powder mixture). The Cr content in this diffusion layer rises up to 21 wt.% at the interface to the carbide, which substantiates its higher solubility in the austenitic matrix compared to the ferritic diffusion zone of the pure Cr coating.

Despite these microstructural differences, the Cr-enriched zones of both diffusion coatings together with the carbide layers are considered to serve as a Cr reservoir for the formation and re-healing of a protective oxide scale during exposure to molten solar salt. A more detailed description of the Cr and Ni+Cr coatings on X20 including EPMA analysis is given in a recent publication [50].

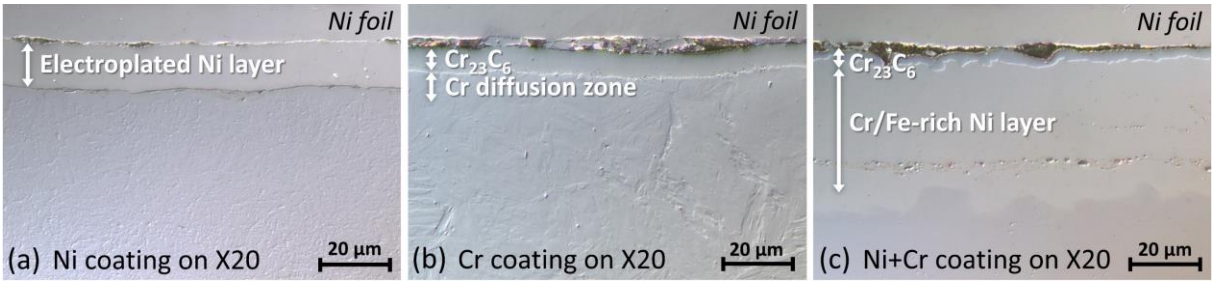

Fig. 2: Cross sections of the three coatings on X20 steel taken by light optical microscope in differential interference contrast (DIC) mode; (a) Ni coating, (b) Cr coating, (c) Ni+Cr coating.

3.2 Corrosion behaviour of pure metals

Results from exposure of pure Ni, Fe and Cr specimens to molten solar salt at 600°C are presented as a background for the interpretation of the corrosion behaviour of substrates and coatings. Fig. 3 shows the evolution of salt chemistry, namely nitrate, nitrite and oxide anion contents, after exposure of blank solar salt and of solar salt surrounding metallic specimens at different time steps.

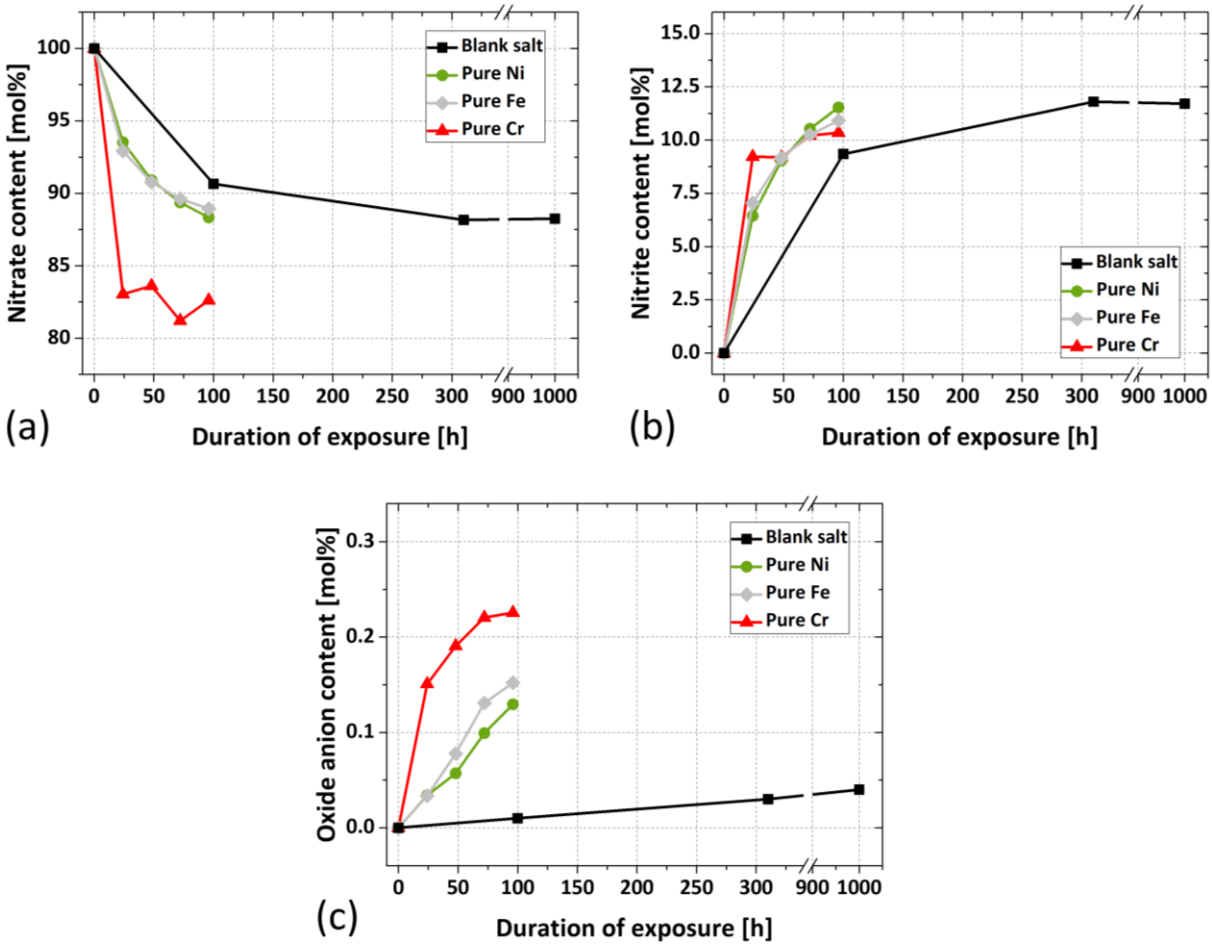

Fig. 3: Changes in salt chemistry over time due to immersion of pure Ni, Fe and Cr specimens in molten solar salt at 600°C; (a) NO_3^- concentration, (b) NO_2^- concentration, (c) O^{2-} concentration. Please note the break in the x-axis of the respective diagrams.

The measured concentration of nitrate anions NO_3^- and nitrite anions NO_2^-, illustrated through Fig. 3a and b, respectively, reveals the formation of a nitrate-nitrite equilibrium (reaction (1)) with ~88 mol% nitrate and ~12 mol% nitrite at 600°C after around 1000 h. The remaining nitrate content is in good agreement with other data presented by the authors of this work [27], but as expected lower than e.g. at 550°C as studied by Villada et al. [2,51]. At the same time, the content of oxide anions O^{2-} (Fig. 3c) increased continuously, which indicates steady decomposition of the salt according to reaction (2). Due to the open test atmosphere under constant air flow (4 l/h), which is accompanied by continuous removal of gaseous NO_X species produced by this reaction, it is expected that the decomposition would progress over time.

Immersion of metallic specimens into molten solar salt clearly altered the salt chemistry as can be particularly well observed after exposure of pure Cr. During the experiment the pure Cr sample was entirely dissolved in the molten nitrate melt after 24 h, producing a bright yellow salt. The salt composition after 24 h reveals that nitrate decomposition was strongly accelerated and the nitrate content (<85 mol%) was already below that of the pure salt in equilibrium (88 mol%). At the same time, the nitrite and oxide ion concentrations after 24 h (9.2 mol% and 0.15 mol%) were significantly higher than in the pure salt. More importantly, a considerable chromate content was measured (up to 8 mol% CrO_4^{2-} from IC measurements, dissolution of Cr in the melt confirmed via AAS). These observations imply that there is a relationship between the rapid change in the salt chemistry and the rapid dissolution of the Cr sample. A possible explanation is that the consumption of metallic Cr during immersion in the liquid melt is accompanied by the consumption of nitrate ions and the formation of nitrite ions as suggested by the following reaction scheme [16,52,53]:

$$2Cr(s) + 7NO_3^- \rightleftharpoons 2CrO_4^{2-} + 3NO_2^- + 3NO_2(g) + NO(g) \quad (3)$$

The overall process illustrated by reaction (3) can be interpreted in different ways. Either metallic Cr is readily converted to chromates through direct reaction with nitrate anions as suggested by Brough et al. [52]. Another mechanism, possibly occurring simultaneously, is the intermediate formation of chromia and its dissolution via basic fluxing according to reaction (4) as proposed in [41].

$$Cr_2O_3(s) + 2O^{2-} + 3/2O_2(g) \rightleftharpoons 2CrO_4^{2-} \quad (4)$$

One can postulate that the rapid Cr dissolution is predominantly driven by the high solubility of the reaction products such as chromates and dichromates in the nitrate melt [54]. These reaction products are constantly removed from the local reaction interface (i.e. sample surface), with the result that continuous decomposition of the Cr sample is maintained until it is completely dissolved.

Such significant changes in the salt chemistry were not observed with the pure Fe and Ni samples immersed in separate crucibles, which show only minor influence on nitrate concentrations compared to pure salt (see Fig. 3a). Different possibilities are worthy of consideration to explain these deviations. Firstly, it is possible that the different salt environments (changing setup, surface/volume ratio, gas flow rate, etc.) had some impact on the nitrate, nitrite and oxide anion composition. Secondly, the formation of oxide scales on pure Fe and pure Ni may have accelerated the nitrate decomposition, thereby causing the release of additional nitrite and oxide anions. In contrast to pure chromium, the changes in the salt chemistry were not accompanied by the dissolution of the immersed metal samples (no traces of Fe or Ni were found in the salt melt within the detection range of AAS). Since Fe oxides and Ni oxide are more resistant to basic fluxing than chromia [55,56], they can be in equilibrium with a higher concentration of oxide anions which might also explain the observed trend. Macroscopic images and cross-sectional BSE micrographs with corresponding element maps after 96 h exposure are shown in Fig. 4. The coupon sample of pure Fe (Fig. 4a) has grown a thick and layered oxide scale under the selected testing conditions.

Evaluation of concentration profiles (not shown here) indicates the formation of mainly hematite, but in some areas up to 19 at.% Na were detected suggesting that sodium iron oxides were partially incorporated within the layered morphology. The scale grown on the pure Ni sample (Fig. 4b) is of significantly smaller thickness (approximately 30 µm versus 150 µm on average) and composed of Ni and O in the ratio 1:1 (in at.%), which suggests the formation of NiO. Unlike the scale grown on the Fe sample, it is less homogeneous and corrosion has propagated through intergranular attack along the grains in the surface region of the Ni specimen. While the formation of rather thick and fast-growing scales on pure Fe is not surprising, the corrosion morphology on pure Ni suggests that its grain boundaries were susceptible to internal oxidation. This unfavourable behaviour could be related to impurities such as carbides present at the grain boundaries. In fact, Bradshaw and Goods [54] reported a similar behaviour of Nickel 200 immersed in molten nitrates at 565°C, which they attributed to its relatively high C content of 0.08 wt.%. Considering the generic order of metals in electromotive force (emf) series, it is likely that such impurities are less noble than the Ni grains (no specific emf series in nitrate melts were found by the authors, but a ranking in chloride melts is given in [57]). Since the Ni specimens used for exposure in the present study are of high purity (99.99%), the resulting cathode (i.e. Ni grains) to anode (i.e. grain boundary impurities) volume ratio is high, which would promote fast anodic dissolution and consequentially intergranular attack. A galvanic coupling effect of carbide precipitates with the Ni-rich matrix of Inconel 600 was recently confirmed in molten chloride melts [58]. However, the relevance of the suggested impurity-driven mechanism cannot be finally proven in our study and will require further investigation.

Despite the formation of a thick scale on pure Fe and the intergranular attack observed on pure Ni, it is essential to emphasise that both metals still showed a higher corrosion resistance compared to pure Cr. This indicates their higher resistance against dissolution in molten solar salt under the prevailing test conditions, which appears to be particularly valid for Ni. Regarding the latter, this is also a valuable hint towards its potentially beneficial properties when employed as alloying and coating element.

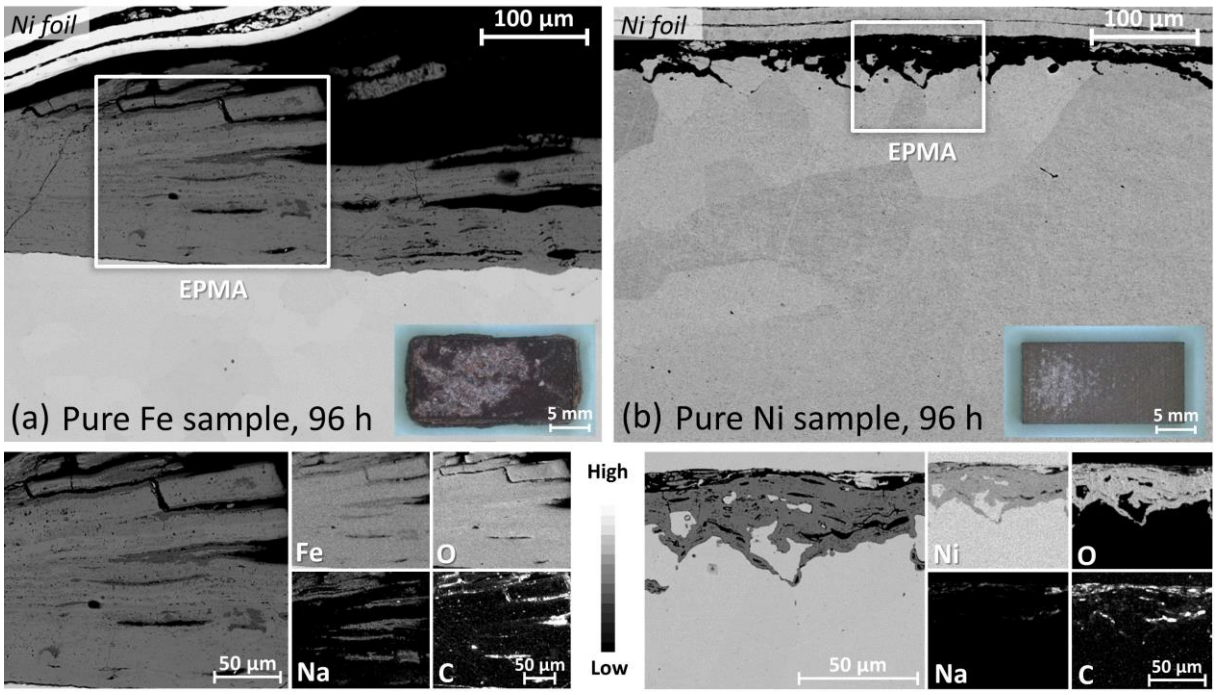

Fig. 4: Cross-sectional back scattered electron (BSE) images and corresponding EPMA element maps of (a) the pure Fe sample and (b) the pure Ni sample after 96 h exposure in molten solar salt at 600°C.

3.3 Corrosion behaviour of alloys and coatings

Fig. 5 shows the net weight change of uncoated and coated X20 and of the reference alloy Haynes 230. Based on the characteristics of the determined curves, 3 different groups can be differentiated:

Uncoated and Ni-coated X20 depict comparatively high net mass gain rates, which decrease over time. Although decreasing mass gain rates are also found with Cr- and Ni+Cr-coated samples, an initial mass loss was detected in both cases. Such a drop within the early exposure stage was previously observed on Cr-coated P91 steel and suggests dissolution of coating components in the molten salt environment [31,59]. It should be noted that this mass loss was found to be higher on the Cr-coated sample than on the Ni-electroplated and chromised Ni+Cr coating. After this initial mass loss, the Ni+Cr-coated specimen indicates a stable behaviour expressed by its comparatively slow mass increase between 100 h and 1000 h. In contrast to all other cases, Ni-base alloy Haynes 230 features a nearly linear mass loss. This behaviour is an indication for continuous dissolution of Cr in the salt as recently reported for Ni-base alloy 625 [25,40,60,61].

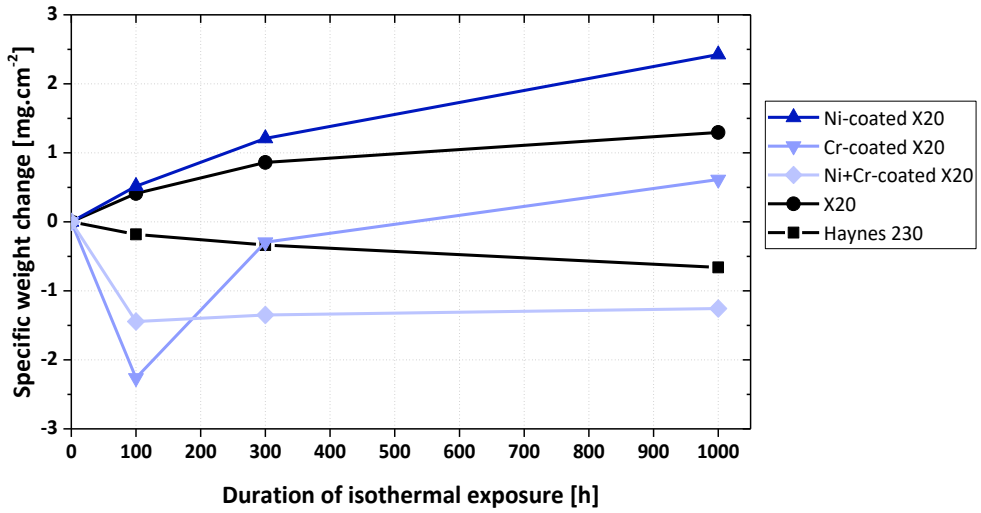

Fig. 5: Specific weight change kinetics of uncoated alloys together with the different coatings on X20 during exposure in molten solar salt at 600°C. Each point indicates the specific weight change of one individual sample.

Salt samples were chemically analysed after immersion of the alloys and coated specimens. Values corresponding to the samples weighed after 100 h exposure (compare results from Fig. 5) are listed in Table 2. Generally, nitrate and nitrite concentrations are in the same order of magnitude as in the reference solar salt. Notwithstanding, it has to be noted that unusual salt decomposition was detected with both the Cr coating and the Ni+Cr coating. Additionally, dissolved chromate ions were found by ion chromatography in both cases (0.08 mol% and 0.03 mol%, respectively).

Table 2: Salt chemistry after immersion of uncoated Haynes 230 and uncoated as well as coated X20 in molten solar salt for 100 h at 600°C. * below detection limit

	Anion content [mol%]			
	NO_3^-	NO_2^-	O^{2-}	CrO_4^{2-}
- (Blank salt)	90.7	9.3	0.01	- *
Haynes 230	91.6	8.4	- *	- *
X20	93.4	6.6	- *	- *
Ni-coated X20	90.2	9.9	- *	- *
Cr-coated X20	89.3	10.6	0.01	0.08
Ni+Cr-coated X20	89.4	10.6	0.01	0.03

Mass change kinetics can be valuable indicators for the type of occurring corrosion mechanisms e.g. oxide growth and scale dissolution. However, since such effects are frequently superimposed and possibly occur together with spallation, mass change characteristics should be evaluated together with further analytical characterisation methods. Hence, for a better understanding of the prevailing corrosion processes, all samples were microstructurally characterised up to 1000 h exposure. The results are discussed in the following sections in the context of mass change kinetics and detected changes in salt chemistry.

3.3.1 Uncoated alloys Haynes 230 and X20

The microstructure of uncoated Haynes 230 and X20 after 1000 h exposure is shown in Fig. 6a and b, respectively. Both alloys are thoroughly discussed in another publication of some of the present study's authors (please see Solimani et al. [62], where corresponding XRD analyses, EPMA maps and concentration profiles are shown). Only a brief summary of their microstructural characteristics is presented here.

The outer part of the scale grown on Haynes 230 after 1000 h exposure (Fig. 6a) consists of a thin NiO layer, which is slightly enriched with Na at the surface. Within the inner layer of the oxide scale $NiCr_2O_4$ and Cr_2O_3 were detected as corrosion products. Underneath the oxide scale, a thin Cr-rich nitridation zone was formed. The presence of such a nitrided sub-surface region underneath the scale agrees with previous findings after immersion of steels and Ni-base materials in molten solar salt and can be associated with N transport to the alloy surface through oxide scale defects [25,30,31].

The oxide scale formed on the uncoated X20 steel after 1000 h exposure (Fig. 6b) shows a striated morphology and consists of a Na-rich outer layer followed by an Fe-rich intermediate layer and a Cr-enriched inner layer. Phase analysis revealed the presence of sodium ferrite ($NaFeO_2$), hematite (Fe_2O_3), magnetite (Fe_3O_4) and wüstite (FeO) as corrosion products. Cr is almost completely absent within the outer and intermediate layers of the scale, which agrees well with the fast dissolution kinetics of the pure Cr sample exposed to solar salt at 600°C and the detection of chromates in the salt as highlighted above. Similar to Haynes 230, N also penetrated the scale/alloy interface where a broad nitridation-affected zone with Cr nitride precipitates within the ferritic matrix is observed. Such precipitates are well-known to be brittle and adversely affect the mechanical properties of steels [63,64].

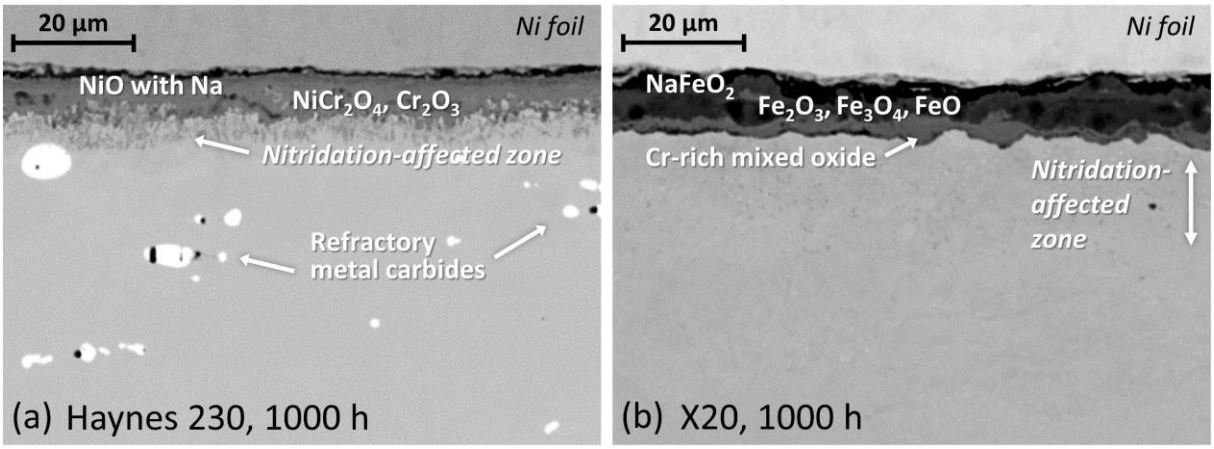

Fig. 6: Cross-sectional back scattered electron (BSE) images of (a) uncoated Haynes 230 and (b) uncoated X20 steel after 1000 h corrosion testing.

On both alloys, the enrichment of Na at the scale surfaces can be attributed to the inward transfer of Na cations from the salt melt to the scale most likely through physical defects in the oxide scale such as pores and cracks [25,31].
It should be mentioned that in the present study Na incorporation into scales was generally observed to be higher than that of potassium. This can be linked to the thermal stability of KNO_3, which was found to be slightly higher compared to that of $NaNO_3$ at the chosen exposure temperature [17,65–67]. Another explanation can be given by the differences in cation sizes of K and Na suggesting that the latter is more mobile since it is slightly smaller (effective ionic radii of 138 pm for K^+ and 116 pm for Na^+, coordination number VI [68]).

3.3.2 Cr coating on X20 steel

Fig. 7a and b show the cross-sectional BSE images and elemental distribution maps as well as concentration profiles of Cr-coated X20 specimens after 100 h and 1000 h molten solar salt exposure at 600°C, respectively. The oxide scale grown on chromised X20 after 100 h has a thickness of nearly 10 µm and exhibits a layered morphology consisting of a Na-rich outer part and an Fe-rich intermediate zone followed by a thin Cr-rich inner layer. Na is enriched at the surface of the scale up to a concentration of nearly 10 at.%, while the Cr concentration at the inner layer reaches 15 at.%. After 1000 h of exposure, the scale thickness increased up to 27 µm and the layered morphology was maintained, while Na was detected almost within the whole oxide scale. Vertical cracks are present among the alternating bands of corrosion products, which were identified as sodium ferrite, hematite, magnetite and wüstite via XRD analysis (see Fig. 10 in the appendix). The presence of such cracks can explain the transfer of Na cations from the salt melt to the scale. As a matter of fact, the extent of Na in the scale increased significantly over time. The presence of a thick $NaFeO_2$ intermediate layer with relatively constant Fe to Na ratio (27 at.% to 14 at.%) suggests that the initially present hematite was continuously enriched in Na during its growth and thereby transformed into sodium ferrite. Similar to the uncoated X20 (see Fig. 6b), a nitridation-affected zone formed under the oxide scale, which can be best observed by the N map in Fig. 7b.

The as-manufactured carbide layer and the Cr diffusion zone (compare Fig. 7 to Fig. 2b) both disappeared after no more than 100 h exposure marking the early consumption of the Cr coating. Since only a thin Cr-rich oxide layer (containing up to 20 at.% Cr) is found at the interface to the slightly Cr-depleted substrate, dissolution of Cr in the salt melt is suspected to be responsible for enhanced Cr loss. This assumption is substantiated by the initial mass loss of the Cr coating as discussed above, the presence of chromates in the molten salt as well as slightly increased concentrations of NO_2^- and O^{2-} (see Table 2). It is also in line with previous studies on Cr-coated P91 steel under similar test conditions [31,59]. For the decomposition of the Cr-rich carbide present in the upper part of the coating similar mechanisms as those discussed for pure Cr (see section 3.2) can be considered. The dissolution of Cr from the carbide layer to the salt will release C formerly bound in the carbide phase. It might either be released to the atmosphere (e.g. through formation of CO gas), form electrolytic compounds (e.g. carbonates) or diffuse back and re-precipitate along the grain boundaries of the substrate (e.g. as carbides such as observed by Fähsing [69] in oxidising, humid atmospheres). In any case, as a result of immediate dissolution,

it can be concluded that the carbide layer does not offer any improved protection compared to the uncoated substrate. It is worth mentioning that in contrast to our observations on chromium carbides, iron carbide phases were recently observed to offer protective properties in molten ternary nitrate and molten ternary carbonate mixtures [28,70]. In these cases, the iron carbides formed during exposure helped to stabilise the corrosion scales grown on the tested alloys, thereby decreasing the corrosion rates.

Our experiments indicate that scales grown on Cr-coated X20 incorporate higher amounts of Na and are considerably thicker than on its uncoated counterpart. This is presumably the result of enhanced release of oxidising species (see NO_2^- and O^{2-} concentrations in Table 2) into the salt melt due to scale and coating degradation according to the aforementioned mechanisms. Subsequently, accelerated oxidation of Fe and its oxides might occur and finally cause the formation of a continuous $NaFeO_2$ scale [71]. This is supported by observations from Sing et al. [72] who report that an increasing concentration of O^{2-} species in the salt, such as detected with the Cr coating, increases the basicity of the melt, which favours incorporation of Na into the scale. Although the diffusion zone underneath the carbide is slightly enriched in Cr (15 wt.% instead of initially 12 wt.%), it might be insufficient for the formation of a slow-growing inner Fe-Cr spinel layer which could inhibit accelerated degradation. This behaviour opposes that of Cr-coated P91 exposed to equivalent test conditions, which proved enhanced corrosion resistance compared to uncoated P91 steel [31]. However, in that study, diffusion zones were much thicker and enriched with up to 20 wt.% Cr. This resulted in the formation of an inner $FeCr_2O_4$ layer, which lowered the corrosion rate significantly compared to uncoated P91. Since in the case of solely chromised X20 no improved corrosion behaviour was achieved and its exposure was concomitant with enhanced Cr loss to the electrolyte, this coating solution disqualifies from use in applications involving contact to molten nitrate salts.

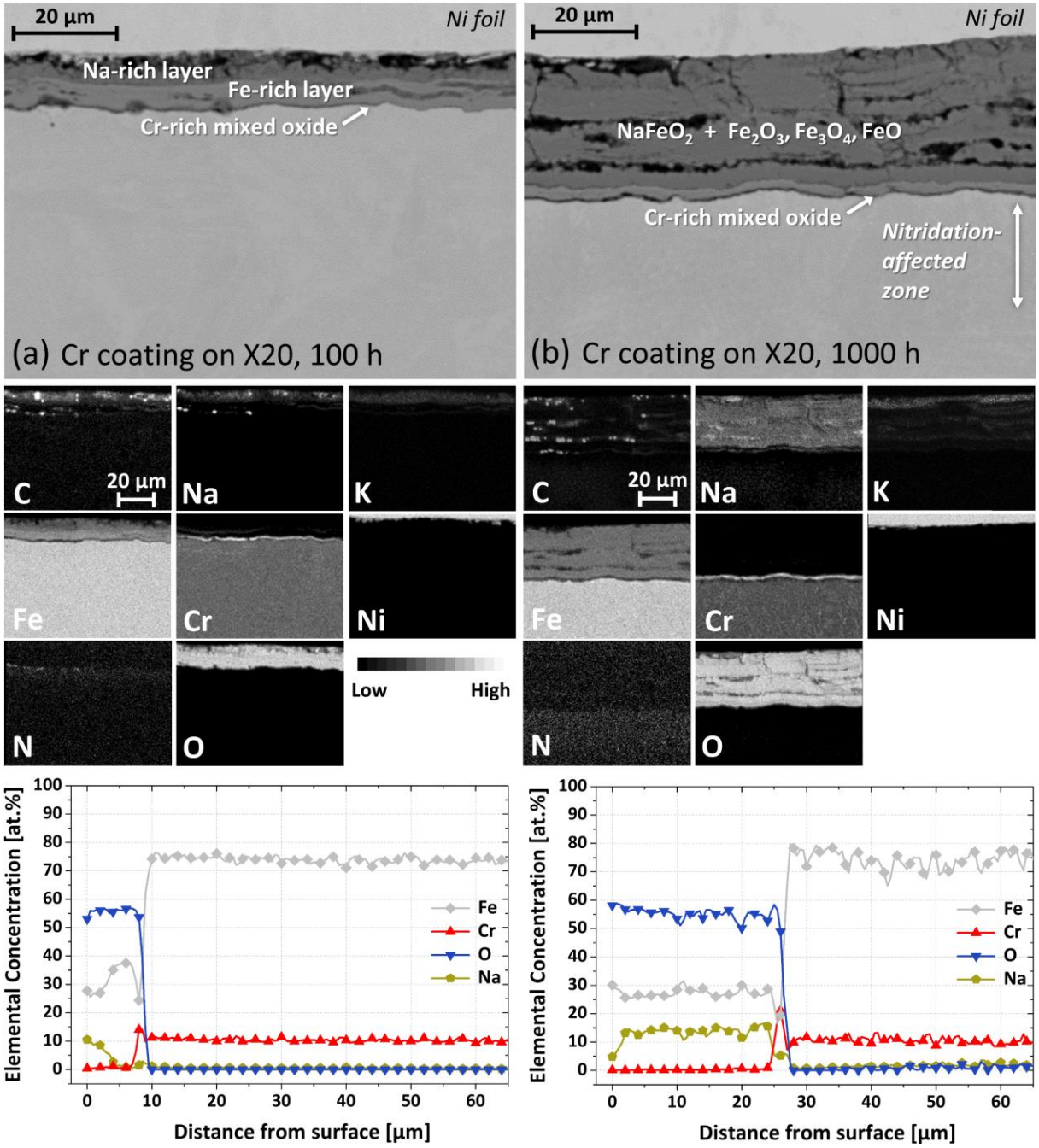

Fig. 7: Cross-sectional back scattered electron (BSE) images, corresponding EPMA element maps and line scans of X20 with Cr coating after (a) 100 h and (b) 1000 h corrosion testing.

3.3.3 Ni coating on X20 steel

Fig. 8a and b show cross sections of the pure Ni coating on X20 exposed to the molten solar salt for 100 h and 1000 h, respectively, together with corresponding EPMA element maps and concentration profiles. Whereas a NiO scale had formed on the Ni-base alloy Haynes 230 (see Fig. 6a), the Ni coating on X20 grew an Fe-rich scale after the initial 100 h exposure, which is still visible after 1000 h but covered with a Na-rich layer of approximately 8 µm thickness. XRD analysis after 1000 h exposure reveals the presence of $NaFeO_2$, Fe_2O_3, Fe_3O_4 and FeO as corrosion products, whereas reflexes belonging to $NaNO_3$ and KNO_3 as well as γ-Ni (coating phase) are also present in the XRD pattern (see Fig. 10 in the appendix). Underneath the multi-layered and Fe-rich scale, an internal oxidation zone formed consisting of oxide branches along the grain boundaries of the electroplated Ni layer. These oxide branches mainly consist of chromia containing some Mn and Fe. Whereas after 100 h only the upper part of the coating is affected, they grew deeper until after 1000 h almost the entire Ni matrix is criss-crossed by such oxide structures. Beyond that, some traces of Na and K were detected in this region. Underneath the initial Ni layer a broad interdiffusion zone has grown, which reaches a depth of 35 µm after 1000 h exposure.

The observed Na enrichment at the surface of the scale and the consequential formation of sodium ferrite originates from Na transport from the salt melt to the salt/scale interface analogous to uncoated and chromised X20. However, the formation of Fe-rich oxides in the early stages of exposure requires considerable outward transport of Fe, which must diffuse from the substrate through the electroplated Ni layer to the corrosion front followed by its oxidation. The outward diffusion of Fe originates from a strong driving force for interdiffusion between the initially pure Ni layer and the steel substrate. Similar observations involving the outward migration of Fe and formation of Fe oxides have been reported for electroless Ni-rich coatings deposited on carbon steel substrates during oxidation tests at temperatures varying between 600°C and 800°C [73,74]. According to these studies, within early stages of exposure a NiO scale forms on electroless Ni-rich coatings, which cannot be maintained for longer durations due to the fast outward transport of Fe from the substrate. Likewise, Ko and Lee [75] have shown the formation of hematite together with NiO and $NiFe_2O_4$ on electroplated Ni coatings on STD61 tool steel during a short time oxidation test (2 to 5 h) at 800°C. Similar to Fe, the outward transport of Cr from the substrate can be confirmed by its presence in the form of oxide branches within the Ni coating. This behaviour can equally be attributed to a steep concentration gradient between the Cr-containing substrate and the formerly Cr-free coating, which established a high driving force for Cr outward migration. At CSP-relevant exposure temperatures (around 600°C) grain boundary diffusion should be the prevailing diffusion mechanism in Ni-rich coatings on steels as reported by Lin et al. [76]. Hence, initial grain size and grain growth during exposure play an important role in the outward diffusion of alloying elements and thus in the formation of scales and precipitates. It is generally accepted that diffusion along grain boundaries is enhanced with decreasing grain size [77]. Fast Fe and Cr outward diffusion through the electroplated Ni layer can thus be associated with the small grain size of the deposited Ni matrix. It has to be taken into account that the pure Ni coatings in this study were not heat-treated prior to exposure in molten solar salt, which might have triggered grain growth reducing the density of grain boundaries as part of the coating manufacturing process.

Compared to Fe, lower oxygen partial pressures are sufficient to oxidise Cr, which explains the preferential internal precipitation of chromia in the coating. The fact that Cr is entirely absent from the scale is a strong indication for its immediate dissolution according to reaction (3) and (4) as soon as it came into contact with the molten salt (when it reached the surface or when the electrolyte penetrated the oxide scale through physical defects). From an electrochemical point of view, galvanic coupling effects should also be taken into consideration. They might play a role in the selective oxidation process of Cr and even Fe when these metals are present in small quantities at the substrate interface which consists of mostly Ni. While an extensive research on emf series in molten solar salt at 600°C is not known to the authors, several studies on galvanic corrosion in halide melts have been published, for instance by Wang et al. [78]. The authors observed that Cr and Fe are the anodes in Ni/Cr and Ni/Fe couples immersed in a molten fluoride salt mixture at 700°C with the largest potential difference between the Ni/Cr couple leading to significant galvanic corrosion of Cr. Although not to be taken for granted in the present study since both electrolyte and exposure temperature are different, such electrochemical considerations support the suggested preferential dissolution of Cr as the most active alloying element.

Degradation as described above caused early coating failure. As a consequence of strong interdiffusion and selective oxidation/dissolution, a protective NiO scale as observed on Haynes 230 Ni-base material (compare Fig. 6a) couldn't grow to protect the ferritic-martensitic substrate from corrosion. Hence, the pure Ni coating must be ruled out as a solution due to the formation of non-protective Fe-rich oxides and intergranular attack. Similar to the intergranular attack observed on the pure Ni sample after exposure in solar salt (see Fig. 4b), the grain boundaries of the deposited Ni layer were preferentially oxidised due to the enrichment of substrate elements via interdiffusion. Nonetheless, it has to be emphasised that Ni itself remained nearly unaffected from corrosion in the reported cases. This is well in line with electrochemical considerations as mentioned above, which predict a more stable behaviour of Ni in comparison to Fe and Cr.

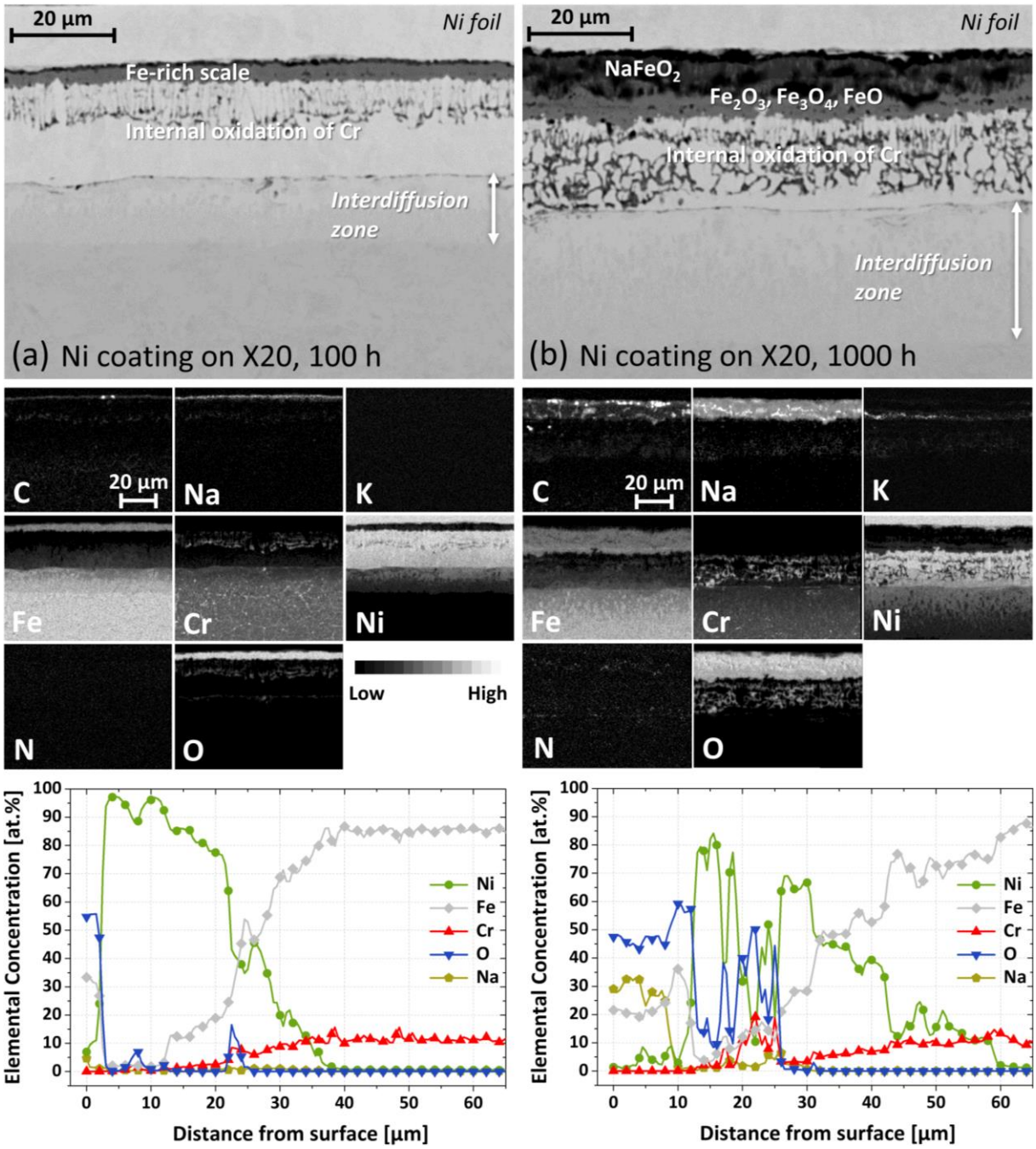

Fig. 8: Cross-sectional back scattered electron (BSE) images, corresponding EPMA element maps and line scans of X20 with Ni coating after (a) 100 h and (b) 1000 h corrosion testing.

3.3.4 Ni+Cr coating on X20 steel

Fig. 9a and b illustrate the morphology of the Ni+Cr coating after 100 h and 1000 h exposure, respectively. Additionally, corresponding EPMA element maps and concentration profiles are shown. The scale grown after 100 h consists solely of a thin Ni-rich oxide. As previously observed on the pure Cr coating (compare Fig. 7a), the former $Cr_{23}C_6$ layer present in the as-coated condition was entirely consumed after this exposure time. Initial mass loss (compare Fig. 5) and small amounts of chromates detected in the salt melt after exposure (see Table 2) corroborate the preferential Cr dissolution discussed in the previous sections. However, the austenitic zone underneath the Ni-rich scale is nearly unaffected and still considerably rich in Cr. Investigation of the coating morphology after 1000 h exposure reveals continuous growth of the Ni-rich scale over time. It has become more complex in composition: Its upper part consists of NiO (slightly enriched in Fe to a maximum of 12 at.%), while its lower part comprises a distinct layer with up to 24 at.% Cr. XRD analysis (see Fig. 10 in the appendix) confirms the presence of NiO, $NiCr_2O_4$, Cr_2O_3 and Fe_2O_3 as the corrosion products together with the γ-Ni as the austenitic coating phase. As a matter of fact, the XRD pattern of Ni+Cr-coated X20 is almost analogous to Haynes 230 with the only exception of the presence of hematite within the scale grown on Ni+Cr-coated X20. Considering the low intensity of the Fe_2O_3 reflexes in the XRD pattern compared to other oxide phases and the relatively low Fe content at the surface of the scale, hematite can only be present in the oxide scale to a very small extent. Apart from its minor incorporation in the scale which required some Fe outward diffusion, hardly any interdiffusion between the austenitic diffusion zone and the ferritic-martensitic substrate occurred during exposure (compare cross sections in the as-manufactured condition, Fig. 2c, and after 100 h and 1000 h immersion, Fig. 9a and b).

Comparison to the pure Ni coating shows that the corrosion resistance of the Ni+Cr coating is substantially higher suggesting that the limited interdiffusion during exposure plays a key role in its corrosion behaviour. The clearly lower extent of interdiffusion can be attributed to the heat treatment provided during the pack cementation process (2 h at 1050°C) and the consequential enrichment of the Ni layer with Cr and Fe by solid state diffusion. This preceding interdiffusion leads to the reduction of concentration gradients between substrate and coating, which, compared to the pure Ni coating, limits the driving force for further interdiffusion during molten salt exposure significantly. In addition, the grains of the Ni+Cr coating phase are substantially larger than those inside the pure Ni coating (which is particularly well visible through comparison of the BSE micrographs in Fig. 9b and Fig. 8b). Since it is unlikely that the molten nitrate exposure at 600°C would cause considerable grain growth, the presence of such large austenitic grains must be attributed to their formation during pack cementation. These large γ-grains provide clearly fewer diffusion paths along their boundaries than those of the Ni coating. Consequently, outward diffusion of alloying elements such as Fe and Cr is much slower and the formation of non-protective oxide scales as well as internal oxidation is successfully inhibited.

Although the discussion of the previous sections highlights the rather negative influence of Cr on alloy and coating corrosion behaviour (Cr and carbide dissolution, formation of chromates, acceleration of corrosive attack), it evidently enhances the resistance of the Ni+Cr coating. Firstly, due the enrichment of Cr within the coating a lower Ni content compared to the pure Ni-coated specimen is required to stabilise an austenitic interdiffusion zone according to the Schaeffler Diagram [79]. This as-manufactured austenitic interface acts as a barrier for the outward diffusion

of Fe during molten salt exposure and inhibits the consequential formation of fast-growing Fe-rich oxide phases [73,74]. Secondly, the enrichment of Cr at the surface promotes the formation of Cr-rich oxide phases ($NiCr_2O_4$ and Cr_2O_3) in the inner part of the oxide scale. Such slow-growing and adherent spinel inner layers on chromised P91 [31] and SS347H (17 wt.% Cr) [25] have been found to offer protective properties in molten solar salt at 600°C. Moreover, the austenitic zone still contains up to 14 at.% Cr at the interface to the scale after 1000 h exposure (see Cr profile in Fig. 9b) and thus presents a Cr reservoir for the re-healing of the spinel layer in case of crack formation or spallation. The merely partial consumption of this reservoir phase during exposure reflects limited dissolution of Cr into the electrolytic salt medium, which seems rather counterintuitive due to the high amount of available Cr. Presumably, the compact oxide phases formed on top of the austenitic zone acted as diffusion barriers slowing down the outward migration of Cr and thus its steady dissolution in contact with the salt melt. While being protected from basic dissolution by the over-growing Ni-rich oxide, the internal Cr-rich scales also decreased the mobility of Fe and Ni cations as well as oxygen inward diffusion and thus the overall kinetics of scale formation.

Altogether, a significantly higher corrosion resistance can be achieved via the Ni+Cr coating compared to the other coatings. Microstructural investigation and post-exposure XRD analysis confirm that a corrosion resistance of coated X20 comparable to that of Haynes 230 (see Fig. 6a) can be achieved via the combined use of Ni and Cr. The slow mass increase determined on Ni+Cr-coated X20 steel after the initial carbide dissolution (see Fig. 5) substantiates this observation. When this carbide layer was dissolved, the Ni-rich austenitic zone came in contact with the nitrate melt. With an initial composition of 70 wt.% Ni, 21 wt.% Cr and 7 wt.% Fe, its surface layer has a similar composition as that of Ni-base alloys with respect to their typical Ni and Cr contents (compare Haynes 230: max. 61 wt.% Ni, 22 wt.% Cr and max. 3 wt.% Fe). Prior investigations of Slusser et al. [40] confirmed the positive effect of such high amounts of Ni to decrease corrosion rates on Fe-Ni-Cr and Ni-Cr alloys immersed in nitrate salt (exposure temperatures ranged from 510°C to 705°C). Interestingly, they observed that such Ni-rich alloys perform much better than pure Ni, which is well in line with findings from our study (compare pure Ni, Fig. 4b to the Ni+Cr coating, Fig. 9a after a similar exposure duration or to Haynes 230, Fig. 6a after even longer exposure). Although the authors did not provide any evidence of Cr-rich oxide formation on alloy surfaces, they equally attributed better corrosion resistance and deceleration of scale growth to Cr oxide or Ni-Cr spinel which might have formed sub-surface. It is noteworthy that our observations regarding the growth of thick scales on pure Fe and Ni specimens (Fig. 4) corroborate the two-face behaviour of Cr regarding the improvement of the scaling behaviour of metallic surfaces in contact with molten nitrates. The findings suggest that the lack of Cr is one cause for faster scale growth on both pure metals compared to the uncoated alloys investigated in this study. On the other hand, when present in large amounts, Cr dissolution, accompanied by the formation of hazardous chromates, presents a drawback from an environmental and industrial point of view due to the necessity of salt regeneration. Thus, Ni-based alloys as well as the Ni+Cr coating on X20 can provide a balanced composition for high resistance.

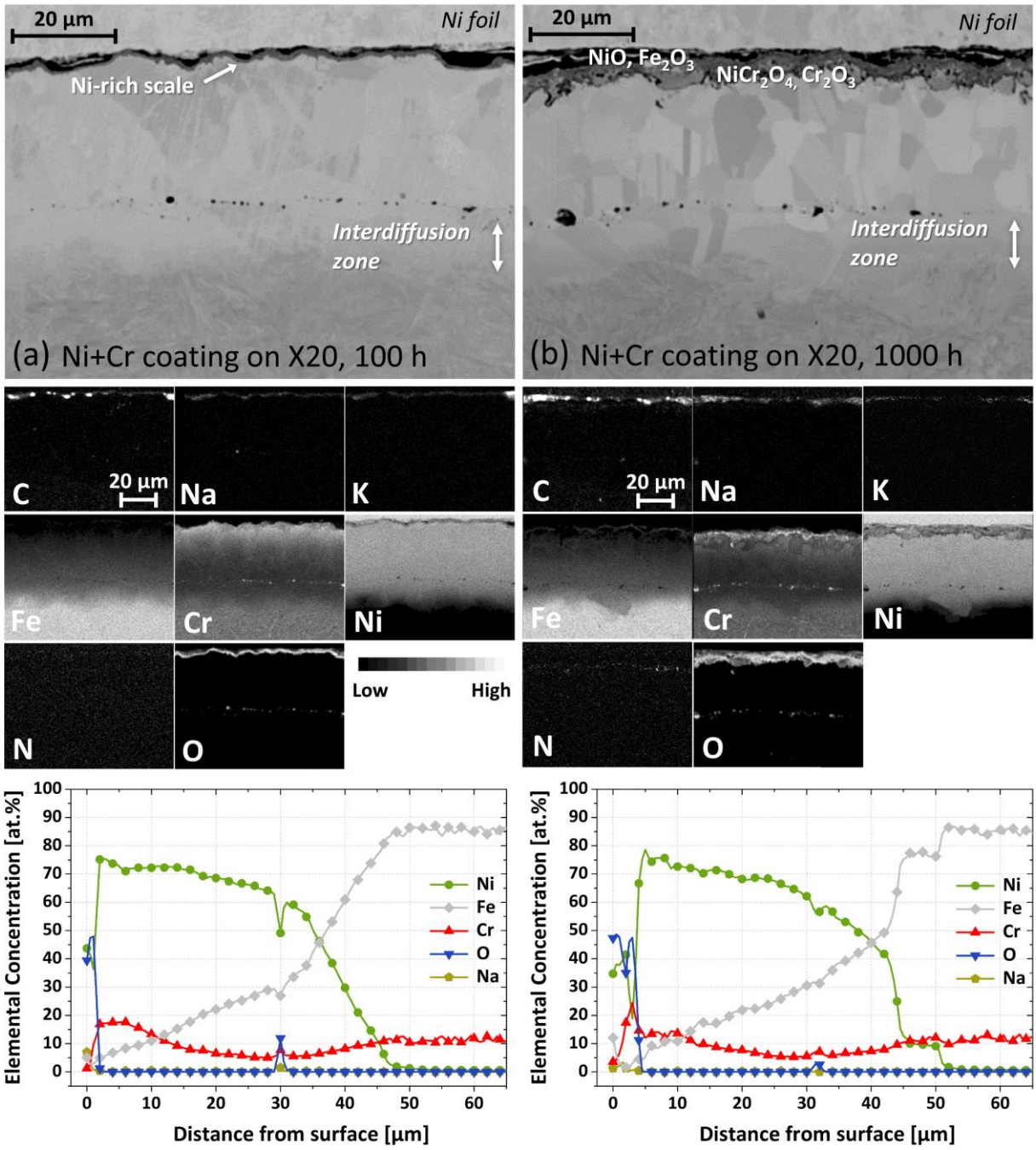

Fig. 9: Cross-sectional back scattered electron (BSE) images, corresponding EPMA element maps and line scans of X20 with Ni+Cr coating after (a) 100 h and (b) 1000 h corrosion testing.

4. Conclusion

The molten salt corrosion behaviour of a pure Ni coating, a Cr diffusion coating as well as a combined Ni+Cr diffusion coating on ferritic-martensitic X20CrMoV12-1 substrate was studied by immersion of test specimens in molten solar salt at 600°C for up to 1000 h. For comparison, the uncoated X20 steel and the Ni-base alloy Haynes 230 were investigated as well. Simultaneously, samples of pure Cr, Fe and Ni were exposed under equal test conditions to elucidate their role as major alloying elements and coating components. The findings can be summarised as follows:

- The specimen of pure Cr dissolved entirely in the molten solar salt in less than 24 h and significantly accelerated the decomposition of the salt mixture. Such an effect is not observed after even longer exposure times up to 100 h with pure Fe (which grows a thick and layered oxide scale) and Ni (which shows some intergranular attack but is less corroded than Fe). The divergent corrosion behaviour of the pure metals provides informative insight into appropriate material and coating selection strategies.
- On uncoated X20 steel non-protective, Fe- and Na-rich corrosion products were formed, while Haynes 230 grew a thin NiO scale. Instead of parabolic mass gain, linear mass loss was observed on the Ni-base alloy, which reflects the continuous dissolution of Cr in contact with the electrolytic salt melt.
- The three coatings showed very different corrosion resistance: In line with the observed solubility of pure metallic Cr in solar salt, the Cr coating ($Cr_{23}C_6$ top layer and adjacent thin Cr diffusion zone) was entirely consumed after only 100 h exposure followed by the formation of thick and non-protective Na-rich oxide scales.
- Despite the high resistance of the metallic Ni specimen, the electroplated Ni coating offered inferior corrosion resistance even in comparison to the uncoated X20 steel due to considerable interdiffusion with the substrate during exposure.
- In comparison with all coated and uncoated materials tested in this study, the combined Ni+Cr coating showed superior corrosion resistance and was able to maintain the growth of a thin and protective NiO scale after 1000 h exposure. Its higher resistance against molten nitrate corrosion is explained by the combined effects of the heat treatment provided during pack cementation as well as the enrichment of Cr at the surface. The thermal processing, on the one hand, resulted in the formation of an austenitic zone reducing the driving force for interdiffusion during exposure significantly. The additional Cr enrichment, on the other hand, led to the growth of highly adherent inner Cr-rich oxide phases during exposure, which are assumed to decelerate overall scale growth and Cr loss to the electrolyte.

5. Outlook

The present study suggests that coatings comprising significant amounts of Ni can successfully improve the corrosion resistance of ferritic-martensitic structural materials in molten nitrate environments as long as interdiffusion with the substrate during exposure is reduced and intergranular attack is inhibited. As concluded from the present work, even conventionally electroplated Ni layers might be worthy of consideration if combined with an optimised pre-oxidation or heat treatment prior to exposure. Future studies will investigate the applicability of such preconditioned Ni layers deposited on steels with the objective to increase their corrosion resistance in molten nitrate salts and simultaneously reduce the contamination of the heat transfer fluid. Besides, the applicability of industrially well-established Ni-P coatings will be investigated in molten nitrate environments.

Acknowledgement

The results presented here belong to the RAISELIFE project, which has received funding from the European Union's Horizon 2020 research and innovation program under grant agreement No. 686008. The authors would like to thank all project partners of RAISELIFE and our colleagues from the working group High Temperature Materials of the DECHEMA-Forschungsinstitut for their support, in particular Dr. G. Schmidt for EPMA measurements, N. Thuma for metallographic preparation as well as M. Braun and A. Hanke from DLR for conducting experiments and post-analysis of salt samples. Furthermore, the Plansee Group is gratefully acknowledged for providing the Cr raw material used in this work.

Declaration of competing interest

The authors declare that they have no known competing financial interests or personal relationships that could have appeared to influence the work reported in this paper.

Appendix

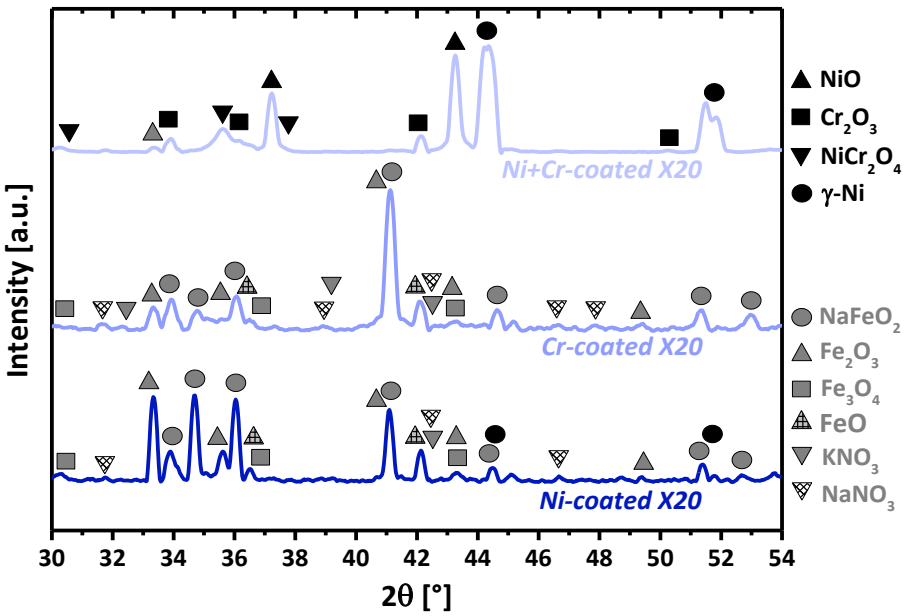

Fig. 10: X-ray diffraction patterns from sample surfaces of the three coatings on X20 (Ni, Cr, Ni+Cr coatings) after 1000 h exposure in molten solar salt at 600°C. The following Powder Diffraction Database (PDF) numbers were used for the reflex identification: NiO: 44-1159, Cr_2O_3: 38-1479, $NiCr_2O_4$: 77-0008, γ-Ni: 04-0850, $NaFeO_2$: 20-1115, Fe_2O_3: 73-2234, Fe_3O_4: 77-1545, FeO: 75-1550, KNO_3: 01-0493, $NaNO_3$: 36-1474.

References

[1] E. González-Roubaud, D. Pérez-Osorio, C. Prieto, Review of commercial thermal energy storage in concentrated solar power plants: Steam vs. molten salts, Renewable and Sustainable Energy Reviews 80 (2017) 133–148.

[2] A. Bonk, S. Sau, N. Uranga, M. Hernaiz, T. Bauer, Advanced heat transfer fluids for direct molten salt line-focusing CSP plants, Prog. Energy Combust. Sci. 67 (2018) 69–87.

[3] C. Ortiz, R. Chacartegui, J.M. Valverde, A. Alovisio, J.A. Becerra, Power cycles integration in concentrated solar power plants with energy storage based on calcium looping, Energy Conversion and Management 149 (2017) 815–829. https://doi.org/10.1016/j.enconman.2017.03.029.

[4] M. Schütze, W.J. Quadakkers, Future Directions in the Field of High-Temperature Corrosion Research, Oxid Met 87 (2017) 681–704. https://doi.org/10.1007/s11085-017-9719-3.

[5] Y. Yoshida, K. Dowaki, Y. Matsumura, R. Matsuhashi, D. Li, H. Ishitani, H. Komiyama, Comprehensive comparison of efficiency and CO_2 emissions between biomass energy conversion technologies—position of supercritical water gasification in biomass technologies, Biomass and Bioenergy 25 (2003) 257–272. https://doi.org/10.1016/S0961-9534(03)00016-3.

[6] A. Boretti, S. Casteletto, S. Al-Zubaidy, Concentrating solar power technology: present status and outlook, Nonlinear Engineering 8 (2019) 10–31.

[7] P. del Río, C. Penasco, P. Mir-Artigues, An overview of drivers and barriers to concentrated solar power in the European Union, Renewable and Sustainable Energy Reviews 81 (2018) 1019–1029.

[8] R.E.H. Sims, H.-H. Rogner, K. Gregory, Carbon emission and mitigation cost comparisons between fossil fuels, nuclear and renewable energy resources for electricity generation, Energy Policy 31 (2003) 1315–1326.

[9] A. Boubault, C.K. Ho, A. Hall, T.N. Lambert, A. Ambrosini, Durability of solar absorber coatings and their cost-effectiveness, Solar Energy Materials and Solar Cells 166 (2017) 176–184.
[10] A. Hall, A. Ambrosini, C.K. Ho, Solar Selective Coatings for Concentrating Solar Power Central Receivers, Advanced Materials & Processes 170 (2012).
[11] R. Reoyo-Prats, A.C. Plaza, O. Faugeroux, B. Claudet, A. Soum-Glaude, C. Hildebrandt, Y. Binyamin, A. Agüero, T.M. Meiβner, Accelerated aging of absorber coatings for CSP receivers under real high solar flux - Evolution of their optical properties, Solar Energy Materials and Solar Cells 193 (2019) 92–100. https://doi.org/10.1016/j.solmat.2018.12.030.
[12] K. Vignarooban, X. Xu, A. Arvay, K. Hsu, A.M. Kannan, Heat transfer fluids for concentrating solar power systems: A review, Applied Energy 146 (2015) 383–396.
[13] C.S. Turchi, J. Vidal, M. Bauer, Molten salt power towers operating at 600–650 °C: Salt selection and cost benefits, Solar Energy 164 (2018) 38–46. https://doi.org/10.1016/j.solener.2018.01.063.
[14] M. Mehos, C. Turchi, J. Vidal, M. Wagner, Z. Ma, Ho,C. ,Kolb,W., C. Andraka, A. Kruizenga, Concentrating Solar Power Gen3 Demonstration Roadmap, Technical Report NREL/TP-5500-67464 (2017).
[15] M. Walczak, F. Pineda, A.G. Fernández, C. Mata-Torres, R.A. Escobar, Materials corrosion for thermal energy storage systems in concentrated solar power plants, Renewable and Sustainable Energy Reviews 86 (2018) 22–44.
[16] A. Bonk, D. Rückle, S. Kaesche, M. Braun, T. Bauer, Impact of Solar Salt aging on corrosion of martensitic and austenitic steel for concentrating solar power plants, Solar Energy Materials and Solar Cells 203 (2019) 110162. https://doi.org/10.1016/j.solmat.2019.110162.
[17] D.A. Nissen, D.E. Meeker, Nitrate/nitrite chemistry in sodium nitrate-potassium nitrate melts, Inorg. Chem. 22 (1983) 716–721. https://doi.org/10.1021/ic00147a004.
[18] R.W. Bradshaw, R.W. Carling, A review of the chemical and physical properties of molten alkali nitrate salts and their effect on materials used for solar central receivers, Proc.Electrochem.Soc. (1987) 959–969.
[19] M. Spiegel, J. Mentz, High temperature corrosion beneath nitrate melts, Mater. Corros. 65 (2014) 276–281.
[20] K.L. Summers, Chidambaram. D., Corrosion Behavior of Structural Materials for Potential Use in Nitrate Salts Based Solar Thermal Power Plants, J. Electrochem. Soc. 164 (2017) 5357–5363.
[21] P.J. Ennis, W.J. Quadakkers, High Chromium Martensitic Steels - Microstructure, Properties and Potential for Further Development, VGB PowerTech 8 (2001) 87–90.
[22] L. Tan, D.T. Hoelzer, J.T. Busby, M.A. Sokolov, R.L. Klueh, Microstructure control for high strength 9Cr ferritic–martensitic steels, Journal of Nuclear Materials 422 (2012) 45–50. https://doi.org/10.1016/j.jnucmat.2011.12.011.
[23] S. Dryepondt, Y. Zhang, B.A. Pint, Creep and corrosion testing of aluminide coatings on ferritic–martensitic substrates, Surf. Coat. Technol. 201 (2006) 3880–3884. https://doi.org/10.1016/j.surfcoat.2006.07.258.
[24] J. Vanaja, K. Laha, M.D. Mathew, Effect of Tungsten on Primary Creep Deformation and Minimum Creep Rate of Reduced Activation Ferritic-Martensitic Steel, Metall and Mat Trans A 45 (2014) 5076–5084. https://doi.org/10.1007/s11661-014-2472-1.
[25] A. Soleimani-Dorcheh, R.N. Durham, M.C. Galetz, Corrosion behavior of stainless and low-chromium steels and IN625 in molten nitrate salts at 600°C, Solar Energy Materials and Solar Cells 144 (2016) 109–116. https://doi.org/10.1016/j.solmat.2015.08.011.

[26] T.-C. Ong, M. Sarvghad, K. Lippiatt, L. Griggs, H. Ryan, G. Will, T.A. Steinberg, Review of the solubility, monitoring, and purification of impurities in molten salts for energy storage in concentrated solar power plants, Renewable and Sustainable Energy Reviews 131 (2020) 110006. https://doi.org/10.1016/j.rser.2020.110006.
[27] A. Bonk, M. Braun, V.A. Sötz, T. Bauer, Solar Salt - Pushing an old material for energy storage to a new limit, Applied Energy 262 (2020) 114535.
[28] M. Gonzalez, U. Nithiyanantham, E. Carbó-Argibay, O. Bondarchuk, Y. Grosu, A. Faik, Graphitization as efficient inhibitor of the carbon steel corrosion by molten binary nitrate salt for thermal energy storage at concentrated solar power, Solar Energy Materials and Solar Cells 203 (2019) 110172. https://doi.org/10.1016/j.solmat.2019.110172.
[29] A. Agüero, P. Audigié, S. Rodríguez, V. Encinas-Sánchez, M.T. de Miguel, F.J. Pérez, Protective coatings for high temperature molten salt heat storage systems in solar concentration power Plants, AIP Conference Proceedings 2033 (2018). https://doi.org/10.1063/1.5067095.
[30] P. Audigié, V. Encinas-Sánchez, M. Juez-Lorenzo, S. Rodríguez, M. Gutiérrez, F.J. Pérez, A. Agüero, High temperature molten salt corrosion behavior of aluminide and nickel-aluminide coatings for heat storage in concentrated solar power plants, Surf. Coat. Technol. 349 (2018) 1148–1157.
[31] C. Oskay, T.M. Meiβner, C. Dobler, B. Grégoire, M.C. Galetz, Scale Formation and Degradation of Diffusion Coatings Deposited on 9% Cr Steel in Molten Solar Salt, Coatings 9 (2019). https://doi.org/10.3390/coatings9100687.
[32] A. Soleimani-Dorcheh, M.C. Galetz, Slurry aluminizing: A solution for molten nitrate salt corrosion in concentrated solar power plants, Solar Energy Materials and Solar Cells 146 (2016) 8–15.
[33] P.F. Tortorelli, P.S. Bishop, J.R. DiStefano, Selection of corrosion-resistant materials for use in molten nitrate salts, Oak Ridge National Lab., TN (USA).
[34] J.W. Cohron, Y. Lin, R.H. Zee, E.P. George, Room-temperature mechanical behavior of FeAl: effects of stoichiometry, environment, and boron addition, Acta Materialia 46 (1998) 6245–6256. https://doi.org/10.1016/S1359-6454(98)00254-7.
[35] R.W. Clark, J.D. Whittenberger, Thermal Expansion of Binary CoAl, FeAl and NiAl Alloys, in: T.A. Hanh (Ed.), Proceedings of the Eighth International Thermal Expansion symposium, 1981, pp. 189–196.
[36] Y.S. Touloukian, R.K. Kirby, R.E. Taylor, P.D. Desai, Thermal expansion of metallic elements and alloy, Plenum Publishing Corporation, New York, 1970.
[37] X. Montero, M.C. Galetz, M. Schütze, Innovative heat treatment and novel non-harmful slurries for "in situ" aluminization or Co-deposition of elements on steels for corrosion protection at high temperatures, in: International Corrosion Conference Series, 2014.
[38] B.L. Bates, Y. Zhang, S. Dryepondt, B.A. Pint, Creep behavior of pack cementation aluminide coatings on Grade 91 ferritic–martensitic alloy, Surf. Coat. Technol. 240 (2014) 32–39. https://doi.org/10.1016/j.surfcoat.2013.12.008.
[39] X. Hou, H. Zhang, M. Seraffon, A.T. Fry, Steam oxidation and mechanical performance of a ferritic–martensitic steel with slurry aluminide coating, Mater. Corros. (2020). https://doi.org/10.1002/maco.202011554.
[40] J.W. Slusser, J.B. Titcomb, M.T. Heffelfinger, B.R. Dunbobbin, Corrosion in Molten Nitrate-Nitrite Salts, JOM 37 (1985) 24–27. https://doi.org/10.1007/BF03259692.
[41] R.A. Rapp, K.S. Goto, The hot corrosion of metals by molten salts, in: R. Selman, J. Braunstein (Eds.), Second International Symposium on Molten Salts, Electrochemical Society, 1981, pp. 159–177.

[42] pauly STAHLHANDEL, Steel Material-Nr.: 1.4922 Data Sheet. https://pauly-stahlhandel.com/wp-content/uploads/2018/02/1.4922.pdf (accessed 2020/05).
[43] Haynes International, HAYNES® 230® alloy, Brochure, 2020. http://haynesintl.com/docs/default-source/pdfs/new-alloy-brochures/high-temperature-alloys/brochures/230-brochure.pdf?sfvrsn=ae7229d4_78 (accessed 2020/05).
[44] C. Duret, R. Pichoir, Protective Coatings for High Temperature Materials: Chemical Vapour Deposition and Pack Cementation Processes, in: E. Lang (Ed.), Coatings for High Temperature Applications, Applied Science Publishers, London, 1983, pp. 33–78.
[45] G.W. Goward, Protective Coatings for High Temperature Alloys: State of Technology, in: Proceedings of the Symposium on Properties of High-Temperature Alloys with Emphasis on Environmental Effects, New York, 1976.
[46] R. Mevrel, C. Duret, R. Pichoir, Pack cementation processes, Mater. Sci. Technol. 2 (1986) 201–206.
[47] ISO 17245: Corrosion of metals and alloys - Test method for high temperature corrosion testing of metallic materials by immersing in molten salt or other liquids under static conditions, ISO TC156 WG 13 (High Temperature Corrosion).
[48] A. Bonk, M. Braun, A. Hanke, J. Forstner, D. Rückle, S. Kaesche, V.A. Sötz, T. Bauer, Influence of different atmospheres on molten salt chemistry and its effect on steel corrosion, in: SolarPACES 2017: International Conference on Concentrating Solar Power and Chemical Energy Systems, Santiago, Chile, AIP Publishing, 2018, p. 90003.
[49] L. Zancheva, M. Hillert, N. Lange, S. Seetharaman, L.-I. Staffansson, On the Formation of Carbide Coatings by Chromizing Carbon Steels, Metall. Trans. A 9A (1978) 909–915.
[50] T.M. Meiβner, X. Montero, D. Fähsing, M.C. Galetz, Cr diffusion coatings on a ferritic-martensitic steel for corrosion protection in KCl-rich biomass co-firing environments, Corros Sci 164 (2020) 108343.
[51] C. Villada, A. Bonk, T. Bauer, F. Bolívar, High-temperature stability of nitrate/nitrite molten salt mixtures under different atmospheres, Applied Energy 226 (2018) 107–115. https://doi.org/10.1016/j.apenergy.2018.05.101.
[52] B.J. Brough, D.H. Kerridge, S.A. Tariq, Molten lithium-potassium nitrate eutectic: The reactions of some compounds of chromium, Inorganica Chimica Acta 1 (1967) 267–270. https://doi.org/10.1016/S0020-1693(00)93183-9.
[53] D.H. Kerridge, S.A. Tariq, Molten sodium nitrite-potassium nitrite eutectic: the reactions of some compounds of chromium, Inorganica Chimica Acta 3 (1969) 667–670. https://doi.org/10.1016/S0020-1693(00)92574-X.
[54] R.W. Bradshaw, S.H. Goods, Corrosion of Alloys and Metals by Molten Nitrates, 2001.
[55] R.A. Rapp, Chemistry and electrochemistry of hot corrosion of metals, Journal of Molecular Liquids 87 (1987) 319–327.
[56] R.A. Rapp, Hot corrosion of materials: a fluxing mechanism?, Corros Sci 44 (2002) 209–221.
[57] H.C. Gaur, H.L. Jindal, Standard electrode potentials in molten chlorides, Electrochimica Acta 13 (1968) 835–842. https://doi.org/10.1016/0013-4686(68)85016-9.
[58] B. Grégoire, C. Oskay, T.M. Meißner, M.C. Galetz, Corrosion mechanisms of ferritic-martensitic P91 steel and Inconel 600 nickel-based alloy in molten chlorides. Part I: NaCl–KCl binary system, Solar Energy Materials and Solar Cells 215 (2020) 110659. https://doi.org/10.1016/j.solmat.2020.110659.
[59] D. Fähsing, C. Oskay, T.M. Meiβner, M.C. Galetz, Corrosion testing of diffusion-coated steel in molten salt for concentrated solar power tower systems, Surf. Coat. Technol. 354 (2018) 46–55. https://doi.org/10.1016/j.surfcoat.2018.08.097.

[60] G. McConohy, A. Kruizenga, Molten nitrate salts at 600 and 680°C: Thermophysical property changes and corrosion of high-temperature nickel alloys, Solar Energy 103 (2014) 242–252. https://doi.org/10.1016/j.solener.2014.01.028.
[61] S. Khorsand, A. Sheikhi, K. Raeissi, M.A. Golozar, Hot Corrosion Behavior of Inconel 625 Superalloy in Eutectic Molten Nitrate Salts, Oxid Met 90 (2018) 169–186. https://doi.org/10.1007/s11085-017-9830-5.
[62] A. Solimani, T.M. Meißner, C. Oskay, M.C. Galetz, Electroless Ni-P coatings on low-Cr steels: A cost-efficient solution for solar thermal applications?, Submitted to: Solar Energy Materials and Solar Cells 09/2020.
[63] I.F. Machado, A.F. Padilha, Aging Behaviour of 25Cr-17Mn High Nitrogen Duplex Stainless Steel, ISIJ International 40 (2000) 719–724. https://doi.org/10.2355/isijinternational.40.719.
[64] U.E. Klotz, C. Solenthaler, P.J. Uggowitzer, Martensitic–austenitic 9–12% Cr steels—Alloy design, microstructural stability and mechanical properties, Materials Science and Engineering: A 476 (2008) 186–194. https://doi.org/10.1016/j.msea.2007.04.093.
[65] T. Bauer, D. Laing, R. Tamme, Characterization of Sodium Nitrate as Phase Change Material, Int J Thermophys 33 (2012) 91–104. https://doi.org/10.1007/s10765-011-1113-9.
[66] E.S. Freeman, The Kinetics of the Thermal Decomposition of Potassium Nitrate and of the Reaction between Potassium Nitrite and Oxygen 1a, J. Am. Chem. Soc. 79 (1957) 838–842. https://doi.org/10.1021/ja01561a015.
[67] G.D. Sirotkin, Equilibrium in melts of the nitrates and nitrites of sodium potassium, Russian Journal of Inorganic Chemistry 4 (1959) 1180–1184.
[68] R.D. Shannon, Revised Effective Ionic Radii and Systematic Studies of Interatomic Distances in Halides and Chalcogenides, Acta Cryst A 32 (1976) 751–767. https://doi.org/10.1107/S0567739476001551.
[69] D. Fähsing, Neuartige Diffusionsschichten zum Oxidationsschutz ferritisch-martensitischer Stähle in wasserdampfhaltigen Atmosphären. PhD Thesis, Shaker Verlag, 2016.
[70] Y. Grosu, A. Anagnostopoulos, M.E. Navarro, Y. Ding, A. Faik, Inhibiting hot corrosion of molten Li_2CO_3-Na_2CO_3-K_2CO_3 salt through graphitization of construction materials for concentrated solar power, Solar Energy Materials and Solar Cells 215 (2020) 110650. https://doi.org/10.1016/j.solmat.2020.110650.
[71] A.G. Fernández, M.I. Lasanta, F.J. Pérez, Molten Salt Corrosion of Stainless Steels and Low-Cr Steel in CSP Plants, Oxid Met 78 (2012) 329–348. https://doi.org/10.1007/s11085-012-9310-x.
[72] I.B. Singh, U. Sen, The effect of NaCl addition on the corrosion of mild steel in $NaNO_3$ melt, Corros Sci 34 (1993) 1733–1742. https://doi.org/10.1016/0010-938X(93)90045-I.
[73] S. Eraslan, M. Ürgen, Oxidation behavior of electroless Ni–P, Ni–B and Ni–W–B coatings deposited on steel substrates, Surf. Coat. Technol. 265 (2015) 46–52. https://doi.org/10.1016/j.surfcoat.2015.01.064.
[74] Z. Weiss, High-temperature Oxidation of Iron Covered by Electroless Ni-P Coating: A GDOS Depth Profiling Study, Surf. Interface Anal. 18 (1992) 691–694. https://doi.org/10.1002/sia.740180910.
[75] J.-H. Ko, D.-B. Lee, Oxidation of Ni films electroplated on steel, Met. Mater. Int. 11 (2005) 85–88. https://doi.org/10.1007/BF03027489.
[76] K.-L. Lin, P.-J. Lai, Interdiffusion of the Electroless Ni-P Deposit with the Steel Substrate, J. Electrochem. Soc. 137 (1990) 1509–1513. https://doi.org/10.1149/1.2086702.
[77] R. Bürgel, H. Jürgen Maier, T. Niendorf, Handbuch Hochtemperatur- Werkstofftechnik: Grundlagen, Werkstoffbeanspruchungen, Hochtemperaturlegierungen und -

beschichtungen, fourth., überarbeitete Auflage, Vieweg+Teubner Verlag / Springer Fachmedien Wiesbaden GmbH Wiesbaden, Wiesbaden, 2011.
[78] Y. Wang, H. Liu, C. Zeng, Galvanic corrosion of pure metals in molten fluorides, Journal of Fluorine Chemistry 165 (2014) 1–6. https://doi.org/10.1016/j.jfluchem.2014.05.010.
[79] A.L. Schaeffler, Constitution Diagram for Stainless Steel Weld Metal, Metal Progress 680 (1949).